Exploring the effect of BN and B-N bridges on the photocatalytic performance of semiconductor heterojunctions: Enhancing carrier transfer mechanism

Emerson Coy, Katarzyna Siuzdak, Iwona Grądzka-Kurzaj, Syreina Sayegh, Matthieu Weber, Marcin Ziólek, Mikhael Bechelany, Igor Iatsunskyi

Exploring the Effect of BN and B-N Bridges on the Photocatalytic Performance of Semiconductor Heterojunctions: Enhancing Carrier Transfer Mechanism

Emerson Coy[1*], Katarzyna Siuzdak[2], Iwona Grądzka-Kurzaj[3], Syreina Sayegh[4], Matthieu Weber[5], Marcin Ziółek[3], Mikhael Bechelany[4*], Igor Iatsunskyi[1*]

[1.] *NanoBioMedical Centre, Adam Mickiewicz University, Wszechnicy Piastowskiej 3, 61-614, Poznan, Poland*

[2.] *Centre of Laser and Plasma Engineering, The Szewalski Institute of Fluid-Flow Machinery, Fiszera 14 Str., 80-231 Gdansk, Poland*

[3.] *Faculty of Physics, Adam Mickiewicz University, Uniwersytetu Poznańskiego 2, 61-614 Poznań, Poland.*

[4.] *Institut Européen des Membranes, IEM –UMR 5635, Univ Montpellier, ENSCM, CNRS, Montpellier, France*

[5.] *Univ. Grenoble Alpes, CNRS, Grenoble INP, LMGP, 38000 Grenoble, France*

Corresponding authors*: coyeme@amu.edu.pl, mikhael.bechelany@umontpellier.fr, igoyat@amu.edu.pl .

Abstract:

Several strategies are currently available to improve the photocatalytic response and performance of materials and devices. Despite this, the most common strategies are still based on the promotion of efficient carrier transfer/lifetime of photo-exited electrons and bandgap tailoring. In this work, we present conclusive experimental evidence of the synergistic effect of Boron Nitride (BN) and B-N bridges on the carrier transfer efficiency of photogenerated species. We present a simple method for exploiting both approaches by the incorporation of B-N bridges on TiO_2/ZnO heterojunctions by Atomic Layer Deposition (ALD). We show the improved lifetime of holes by the integration of B-N bridges, as shown by the very low first-order recombination times 3.4±1.2 ns^{-1}, and the superior photoresponse of the composites, with a strong increment of 170% observed in transient photocurrent studies and supported by the incident photon to current efficiency. Also, the TiO_2/ZnO/BN heterojunction presents an 82% in photodegradation of contaminants (k=7.84*10^{-3} min^{-1}). Finally, we provide experimental evidence of the hole extracting role of BN and bring a general strategy for integration of B-N bridges by ALD conformal coating capabilities. We believe that the results open up the possibility for exploitation in several architectures, materials, and devices by in-situ preparation of efficient carrier transfer layers by ALD.

Key Words: Photocatalysts; Water splitting; Atomic Layer Deposition; Metal Oxides; Boron Nitride.

1. Introduction

The search for efficient, environmentally safe, and reusable photocatalysts for clean energy production and environmental remediation is one of the most actively researched topics to date[1]. Currently, studies on photocatalyst include several semiconductor materials from a wide variety of chemical families, including sulfides[2,3], selenides [4], among others[5,6]. Despite the wide variety of novel materials explored in the literature, metal oxides still gather much attention due to their easy integration with current technology and broad scope of application, such as photovoltaic devices[7], electronics[8], protective coatings[9] and energy production [10]. Two of the most studied oxides are titanium dioxide (TiO_2) and zinc oxide (ZnO). These ceramic materials have shown robust stability in both liquid and dry conditions[11,12], many different synthesis methodologies, and a wide variety of nanostructures[11,13–15]. Moreover, these materials have shown a rather tunable direct bandgap, which is located in the near-ultraviolet region, at 390 nm (3.2 eV)[16] and 375 nm at (3.3 eV)[17] for TiO_2 and ZnO, respectively. Additionally, both materials have shown high bio-compatibility[7,18,19] and low environmental risk [20,21], making them ideal for the study of electron transfer mechanism in prototyping photocatalysis[22,23] with real potential for implementation in contaminated or heavily polluted environments[24–26].

Despite their high interest and broad application of TiO_2 and ZnO, much research is still focusing on understanding their electronic and optical response at the nanoscale, especially when using dopants[27,28] and in heterojunctions with other semiconductors or metals[29–32]. Previously, we have studied the electron transfer mechanism, optical, mechanical, and electronic tunability of several photoactive nanostructures, including nanolaminates of ZnO/Al_2O_3 [33,34], TiO_2/Al_2O_3, and other photocatalyst systems based on ZnO and TiO_2[34,35]. Additionally, we have recently shown that the interface of TiO_2/ZnO provides an efficient method for charge separation of photogenerated electron-hole pairs improving the catalytic performance of $Si/TiO_2/ZnO$ nanopillars[36]. Despite the promising results obtained in the TiO_2/ZnO interface, when compared to their single-layer counterpart, the nanostructures still possess a bandgap of >3.6 eV (<344 nm) residing close to the lower end of the visible spectra, but still in the near UV region. Therefore, further research is necessary to exploit the improved charge separation of the composite, while shifting the bandgap towards the visible region of the light spectra.

One possible strategy recently explored in the literature is the combination of Boron Nitride (BN) with semiconductor materials. Studies have shown that BN is excellent electrical properties[37,38], it has also shown to be an initiator in the catalytic conversion of light alkanes[39], highly selective for the propane[40] and ethylbenzene dehydrogenation[41], among other catalytic reactions[42–44]. Furthermore, the combination of semiconductors has shown improved charge

separation and transfer properties, which are especially attractive in the BN-based photocatalysts[45–48]. Moreover, these improved effects become more pronounced when BN is combined with a semiconductor material to create Metal-O-B-N and O-Metal-B-N bridges with the photocatalyst since these bridges are suggested to induce the narrowing of the bandgap in B-N-TiO_2 photocatalytic systems[49,50]. These effects are supported by studies showing the improvement in charge separation and transfer of unreacted TiO_2/BN composites, while the composite with B-N bridges shows a shifting of the bandgap to shorter UV wavelengths[51], also seen in B doped catalysts[52]. Besides, it was shown that the negatively charged BN, as a superior hole extractor, improves the separation of photogenerated charge carriers, and promotes the fast transfer of holes towards the surface[53].

BN can be synthesized in several crystalline forms, being the most useful for photocatalytic applications its hexagonal phase (h-BN), which is in many ways similar to that of graphene[54]. Most of the applications of BN are inherently connected with the nitride family, which are refractory materials (900^{o} C) with strong mechanical properties[55]. Although by itself, BN has no significant electrochemical activity and its wide bandgap makes it not directly applicable in photocatalysis, it has gathered much attention in the field of photonics [56] and energy production, through the so-called, interface engineering [45]. Moreover, since BN is an insulator, it is usually used in electrochemistry as support for photo/electro catalytically active materials[57,58]. Therefore, in order to integrate a layer of BN with the TiO_2/ZnO system, while securing the generation of Metal-O-B-N and O-Metal-B-N bridges, a simple exfoliation or drop-casting transfer method would not be enough. Luckily, recent developments in Atomic Layer Deposition (ALD) have allowed depositing conformal layers of BN layers and nanotubes [59,60], with controlled thickness at high temperature (650-750 °C). This method is much more favorable for triggering Metal-O-B-N and O-Metal-B-N bridges in TiO_2/ZnO while keeping the BN properties intact.

Therefore, in this study we examine the influence of BN and B-N bridges in model photocatalyst TiO_2 and TiO_2/ZnO surfaces by ALD. The samples' surface morphology, crystalline structure, and chemical nature are inspected by Atomic Force Microscopy (AFM), Scanning Electron Microscopy (SEM), Raman spectroscopy, and X-ray Photoelectron Spectroscopy (XPS). The optical properties of the sample are investigated by UV-VIS, while the photoelectrochemical response and the charge transfer mechanism will be studied by Cyclic Voltammetry (CV), Chronoamperometry, Electrochemical Impedance Spectroscopy (EIS), and Transient Absorption Spectroscopy (TAS), respectively. Here, we will show that in-fact ALD allows for the creation of highly photoactive nanocomposite surfaces based on TiO_2/ZnO/BN, with an optical bandgap energy shift to the visible range and superior catalytic performance. Additionally, we will prove that the lifetime of photogenerated electron-hole pairs has been dramatically increased, providing a competitive framework for further development of composite photocatalyst.

2. Experimental

2. 1. Photoanode fabrication: All depositions have been carried out in a horizontal, low-pressure hot-wall (home-built) ALD reactor. More details about this reactor can be found elsewhere[59,61]. Following precursors have been used for deposition: titanium tetrachloride ($TiCl_4$), diethylzinc ($(C_2H_5)_2Zn$), boron tribromide (BBr_3) precursor, water (H_2O), and ammonia gas (NH_3). All precursors were purchased from Sigma Aldrich. As a substrate, quartz glass with an FTO layer (600 um) was used. The typical protocols for TiO_2, ZnO, and BN deposition are described elsewhere[59,61,62]. Briefly, the ALD cycle consisted of 0.5 s of $TiCl_4$ and $(C_2H_5)_2Zn$, 2 s exposure, and 5 s purge of nitrogen, followed by 0.5 s pulse of water. In total, 400 ALD cycles of TiO_2 and 25 cycles of ZnO, corresponding to 20 nm and 5 nm, respectively. The temperature of deposition was 200°C. The typical ALD cycle for BN deposition consisted of 0.1 s pulse of BBr_3, 2 s exposures, and 5 s purges, followed by a 3 s pulse of NH_3, 5 s exposures, and 5 s purges with Argon. Fifty ALD cycles of BN were applied, corresponding to the average thickness of 5 nm. The temperature of deposition was 750°C.

2.2 Characterization: Structural properties of samples were analyzed by scanning electron microscope (SEM) JEOL JSM – 7001F. The GIXRD measurements were performed by X'pert^3 MRD (XL) from PANalytical, working with a Cu Kα radiation source (wavelength of 1.54 Å) and operating at 45 kV and 40 mA. Raman spectroscopy measurements were performed in a Renishaw micro-Raman spectrometer equipped with a confocal microscope (Leica) (excitation wavelength – 514 nm). X-ray photoelectron spectroscopy XPS (ESCALAB 250, ThermoElectron equipped with an Al Kα line 1486.6 eV as monochromatic excitation source with a 400-μm spot size) were used to analyze the chemical composition of the produced samples. Atomic force micrographs (AFM) were collected in an ICON – Bruker microscope. Optical properties of samples have been studied with UV–vis spectrophotometer Lambda 950 UV/VIS/NIR range 300–1100 nm, 1 nm step.

2.3 Photoelectrochemical characterization: Characterization of the working electrode was performed using the potentiostat-galvanostat system AutoLab PGStat 302N in a standard three-electrode assembly at room temperature. The platinum gauze was used as the counter electrode and the Ag/AgCl/0.1 M KCl as the reference electrode. The 0.5 M Na_2SO_4 (pH=7) electrolyte solution was preliminarily deaerated with Ar for 40 min before measurements and the constant solution flow of Ar above the electrolyte was kept during all measurements. The electrochemical cell is equipped with a quartz window. The samples were irradiated with a 150 W Xenon lamp (Oriel LS0500) equipped with an AM 1.5 filter allowing to obtain simulated solar light. The irradiance of incident light was

calibrated to 100 mW/cm^2 using a reference cell (Si solar cell, Rera). The electrochemical impedance spectroscopy (EIS) was measured under the open circuit in the dark and under illumination conditions, and no iR compensation[63], in the frequency range of 0.1–20 kHz at an amplitude of 10 mV results were analyzed and fitted in Z-View software using an electrochemical equivalent circuit (EEQC) composed of a CPE-R circuit, fitted data shows a goodness-of-fit-value (χ^2) below $-10^{-}4$ (see Supplementary section for details). The chronoamperometry measurements were performed under chopped illumination with a 5 s period under polarization conditions +0.5 and + 1.0 V *vs.* Ag/AgCl/0.1 M KCl.

2.4 Photodegradation experiments: The photocatalytic activity was evaluated using Rhodamine 6G solution (5 mg/L) as a model organic dye. Before irradiation, the dye solution and the sample were stirred in the darkness for 30 min to reach adsorption-desorption equilibrium. The UV–Vis light irradiation was carried out in a quartz cuvette using Xe lamp (Lambda LS model LB-LS/OF 30R, 4.5 Watts/300 W) at a distance of 10 cm from the surface of the solution in horizontal geometry. During the reaction, the dye solution was stirred continuously. The absorbance measurements were performed at a regular interval time (30 min). The concentration of rhodamine 6G in the solution was estimated using the absorbance spectrum at λ = 525 nm.

2.5 Femtosecond transient absorption spectroscopy: Transient absorption system (Helios spectrometer, Ultrafast Systems, and Spectra-Physics laser system) has been described in more detail elsewhere[64,65]. The pump laser pulse was set at 310, 355, or 375 nm, and its energy was varied between 0.2 and 8 μJ, corresponding to energy densities between 0.1 and 4 mJ/cm^2, respectively. The IRF (pump-probe cross-correlation function) duration was from 150 to 300 fs (FWHM). The transient absorption measurements were performed in the spectral ranges of 330−650 nm (UV-VIS) and 850−1550 nm (NIR) and in the time range of up to 3 ns.

3. Results and Discussion

3.1 Samples preparation and Physico-chemical characterization

Samples of TiO_2 (20nm)/ZnO (5nm) were prepared according to the protocols described in the Methods section. **Figure 1a** shows a schematic representation of the procedure used in the deposition of the subsequent films resulting in a stacked-like sample. In short, conformal layers of TiO_2 and ZnO were deposited on fluorinated Tin Oxide glasses (FTO) and then subjected to the high-temperature deposition of BN. The BN layer grows coherently on the surface while promoting the specific linkers for the Zn-O-B-N and O-Zn-B-N bridges. After the deposition process, the morphology of the

samples did not show visible changes, the substrates remained transparent and without cracks (**Figure 1b**). SEM and AFM micrographs, **Figure 1c and 1d** respectively, show the rather smooth surfaces and small increment in roughness after the BN deposition, from ~20 nm to ~60 nm, which is associated with the high-temperature process of the BN deposition (**Table S1**). The high roughness of the FTO glasses and a rather low dimension of the layers made the structural determination of the layer by X-ray Diffraction (XRD) unfeasible. However, Raman studies performed on the samples clearly showed the apparition of phonon peak around 145 cm^{-1}, corresponding to the TiO_2 Anatase phase (**Figure 1e**), which is the result of the high-temperature process of the BN deposition.

Despite the lack of structural confirmation by XRD, we can rely on the experience gathered in our previous studies on flat substrates [33–36,59,61,66–69]. Further confirmation of the presence of the BN and Zn-O-B-N bridges can be clearly shown by their influence on the UV-VIS spectra and bandgap of the samples and the stoichiometry of the samples by XPS. **Figure 1f** shows the Tauc plot obtained from optical transmittance spectra of the prepared samples where the clear decrement in bandgap energy is observed in the BN covered samples, from TiO_2 (3.25 eV) and TiO_2/ZnO (3.31 eV) to TiO_2/BN (3.03 eV) and TiO_2/ZnO/BN (3.12 eV). As mentioned before in the introduction section, the mere combination of BN with semiconductor materials, although improving the charge carrier separation and increasing the lifetime, does not narrow the bandgap of the composite[51]. The clear decrement in bandgap energy suggests the appearance of the Zn-O-B-N and O-Zn-B-N bridges in the samples. However, a more conclusive statement can be obtained by XPS, as shown in **Figure 1g and 1h**, by investigating the Boron (B 1s) and Nitrogen (N 1s) core level spectra of both TiO_2/ZnO and TiO_2/ZnO/BN the presence of two clear species confirms the presence of Zn/Ti-O-B-N and O-Zn/TiO-B-N bridges and pure BN. In the boron region, a peak coming from BN is observed (190.6 eV)[70,71] and hybridized secondary peak can be attributed to the Zn-O-B-N and/or O-Zn-B-N (191.8 eV)[71–73]. Moreover, the N1s region, shows the distinctive presence of the nitride peak (398.1 eV)[71,74], with a higher energy secondary peak, that can be attributed to N-C or N-O bridges (399.9 eV)[75]. (Other components in Supplementary Material **Figure S1, S2, and Table S2**).

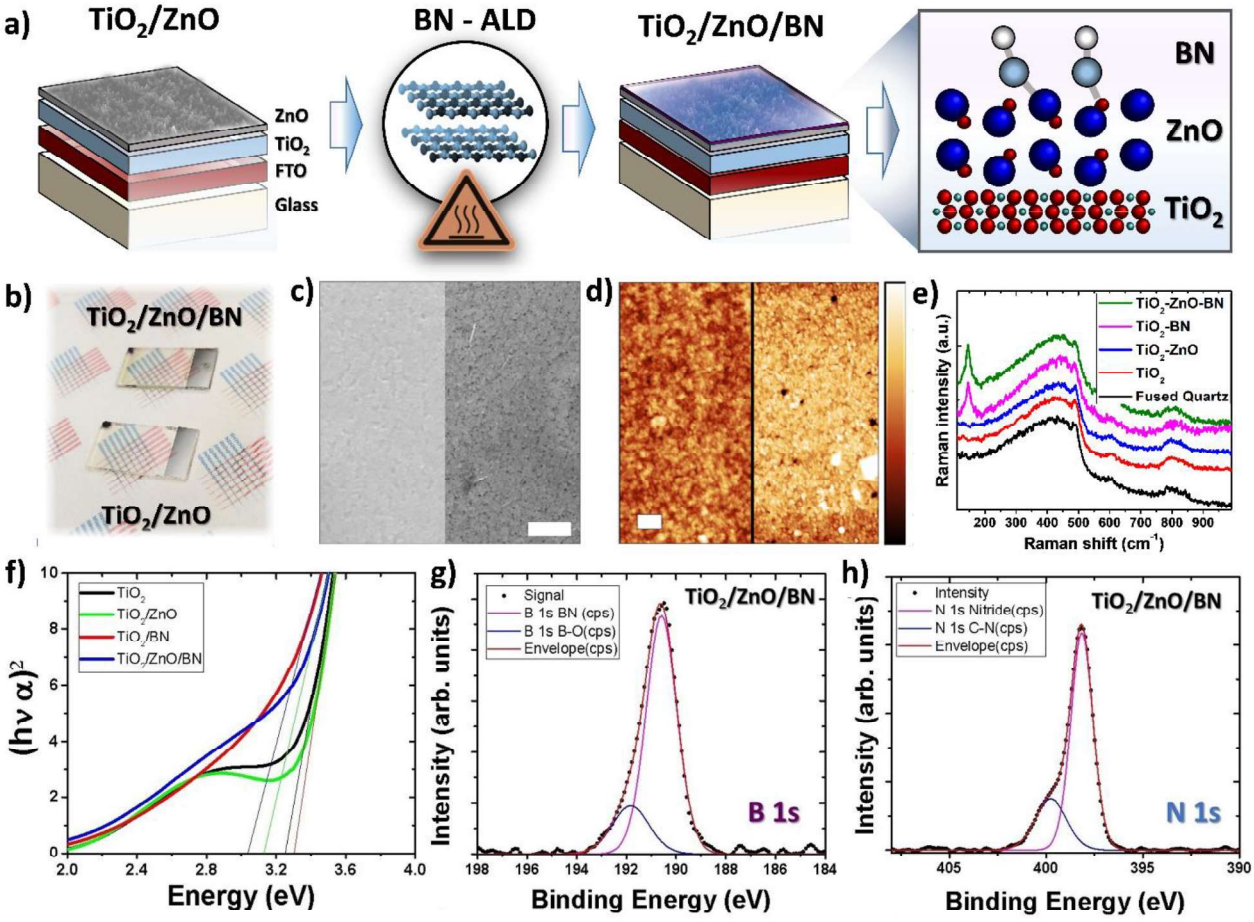

Figure 1: a) Schematic representation of the sample construction prepared in this study. Quartz coated FTO substrates were successively covered by TiO_2, ZnO, and high-temperature BN deposition. The top layer of the schematics shows the rough surfaces of the layers. Finally, the ideal schematic representation of the bounds of BN layers, interaction with the ZnO/TiO_2 **b)** Optical images of the samples with (top) and without (bottom) BN layers. Shaded regions are the clamped sections of the substrate used for manipulation. Patterned background is used to show the transparency of the samples **c)** SEM images of the substrates with ZnO/TiO_2 (left) and after the deposition of BN (right). The scale is 1 µm for both images. **d)** AFM micrographs once again with ZnO/TiO_2 (left) and after the deposition of BN (right). The scale is 1 µm for both images. **e)** Raman spectra for all prepared samples with the clear apparition of E_g for anatase (~145 cm^{-1}) for the B-N deposited samples. **f)** UV-Vis spectra and bandgap estimation for different samples. **g)** High-resolution spectra of the B1s region for $TiO_2/ZnO/BN$ showing the two species of Boron in the samples. **h)** High-resolution spectra of the N 1s region for $TiO_2/ZnO/BN$ with clear distinction of the nitride peak from (BN) and a secondary contribution

3.2 Photoelectrochemical response of TiO_2/ZnO and TiO_2/ZnO/BN heterojunctions.

To investigate the electrochemical response of the samples, we used Cyclic Voltammetry (CV) as shown in **Figure 2a**. It is clear by examining the anodic region of the plots that TiO_2 and TiO_2/ZnO

samples show little activity towards Oxygen Evolution Reaction (OER), especially when compared with the BN-covered samples. A well-defined OER response is observed for both TiO_2/BN and TiO_2/ZnO/BN samples with an onset of 0.7±0.1$V_{Ag/AgCl}$ and +0.6±0.1 $V_{Ag/AgCl}$, respectively. One important aspect that can be observed, is the oxidation shoulder at around +0.4 $V_{Ag/AgCl}$ in the TiO_2/BN sample, a feature that is not present in the TiO_2/ZnO/BN sample, suggesting that ZnO, provides an extra layer of protection towards oxygen physisorption as well as contributing to the superior inertness of the electrode. **Figure 2b and 2c** show LV plots recorded during chopped illumination and chronoamperometric tests respectively. In the chopped illumination, there is little difference between TiO_2 and TiO_2/ZnO samples, while the response is enhanced for TiO_2/BN and TiO_2/ZnO/BN, being the latter the one with the higher performance, especially at higher anodic voltages. Furthermore, **Figure 2c** presents the transient photocurrent recorded for all the samples at E=+0.5$V_{Ag/AgCl}$ during light/dark cycles, the results show the enhancement of the TiO_2/ZnO/BN and confirm the stability of the samples over time. Importantly enough, the response recorders show an increment of 170% for TiO_2/ZnO/BN with respect to the rest of the samples. Notice that the improvement is also in agreement with Incident Photon to Current Efficiency (IPCE) measurements (**Figure S3**), which indicate a 165% higher total photocurrent in TiO_2/ZnO/BN sample over the bare TiO_2/ZnO sample.

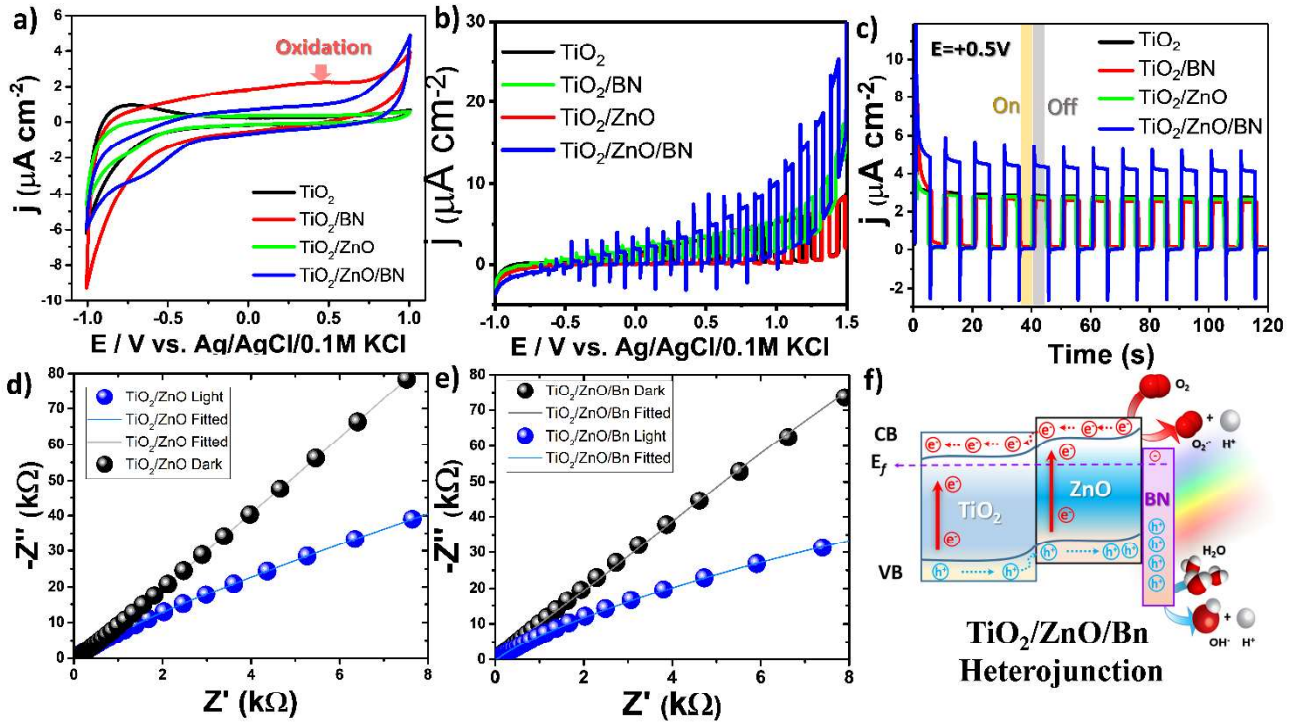

Figure 2: a) Cyclic voltammetry curves of electrodes registered in 0.5 M Na_2SO_4, the red arrow shows the oxidation shoulder. **b)** Linear voltammetry curves of electrodes registered under chopped solar light. **c)** Transient photocurrent of the samples, with the highest photoactivity observed for TiO_2/ZnO/BN (0.5 $V_{Ag/AgCl}$), shaded regions represent on(yellow) off(grey) cycles. Electrochemical

impedance spectroscopy measurements in light/dark conditions for **d)** TiO_2/ZnO and **e)** TiO_2/ZnO/BN. Dots are experimental data while continuous lines are the result of the fitted circuit. **f)** Proposed mechanism for the TiO_2/ZnO/BN sample illustrating the enhanced electron transfer between the TiO_2/ZnO interface and the hole-extraction of the BN surface layer.

The charge transfer dynamics are studied by Electrochemical Impedance Spectroscopy (EIS) in dark/light conditions at open circuit potential. First, the general mechanism response of TiO_2/ZnO was examined by representing the EIS data in the Nyquist plot, which shows an improvement of the charge transfer resistance from 17.8 kΩ to 10.1 kΩ during illumination conditions, see **Figure 2d. Table S1** contains detailed values for the fittings performed on the spectra**.** The results suggest the formation of electron-hole pairs, which lower the electrode resistance**.** The same behavior is observed for TiO_2/ZnO/BN, in this case, the charge transfer resistance is much lower than for the bare sample while changing from 5.9 kΩ to 5.2 kΩ during dark/illumination conditions. As mentioned before, these values are smaller than the observed for the TiO_2/ZnO sample and point to the superior photocatalytic performance of the TiO_2/ZnO/BN heterostructure(**Figure 2e and Table S1**).

The electrochemical results show the higher photoactivity of the TiO_2/ZnO/BN heterostructure, which is explained by the proposed electron transfer mechanism, shown in **Figure 2f**. The TiO_2/ZnO interface allows the photogenerated electrons in ZnO to quickly migrate to the TiO_2 layer, forcing the holes to move toward the ZnO surface, thus reducing their recombination rate. Additionally, the introduction of BN and B-N bridges results in the fast collection of holes at the surface of the composites, which is translated into the efficient OER mechanism recorded in our experiments. The combination of a fast electron transferring interface and a hole-collector surface boosts the general electrochemical performance of the here presented heterojunction.

3.3 Effect of BN layers in and lifetime and carrier transfer mechanism

Having analyzed the structure and the electrochemical response of the samples, we now focus on the lifetimes and the recombination studies of the samples. Transient absorption studies allow the identification of different distinctive species generated under light irradiation. According to the position of such signals in the spectra, we can determine several effects, such as: first, the long-lasting signal below 400 nm (positive absorption rising towards 340 nm, see **Figure S4**) is dominated by the thermal artifacts, which are understood as broadening of the titania absorption band upon local sample heating (**Figure S5**). Secondly, the positive signal between 400 and 650 nm (**Figure S4**) is due to the holes and trapped electrons (but dominated by the holes for the pump energy density range used in this work), while the signal in Near Infra-Red (NIR) range (850-1550 nm, **Figure S6**) is dominated by free and shallowly trapped electrons [76,77]. In short, the ultrafast signals (<0.3 ps) in the UV-

VIS range are obscured by a two-photon absorption artifact in the substrate [64]. **Figures 3a and 3c** show a 2D plot of the wavelength *vs* decaying time, where the clear changes of BN-containing samples are visible. The negative signal in the range from 400-450 nm for the samples with BN probably originates from the bleach induced by the presence of the tail in the absorption spectra (compare with **Figure 2a**).

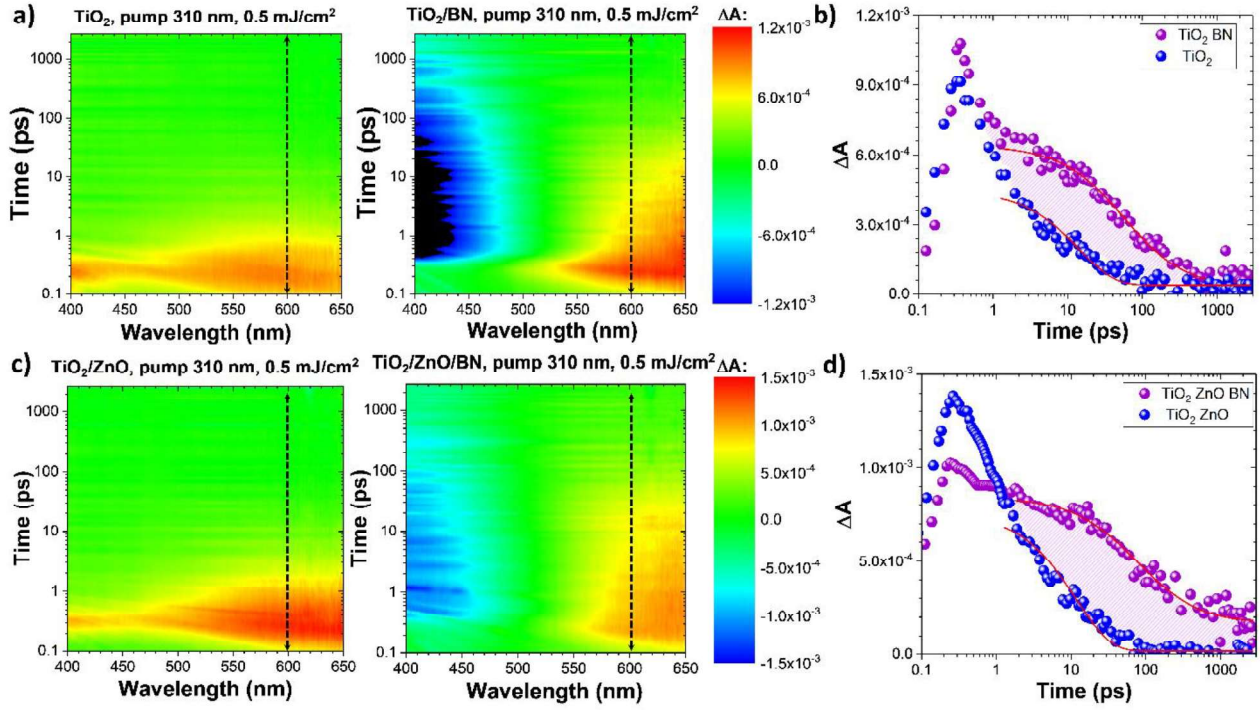

Figure 3: Pseudo-color 2D spectra of transient absorption data for wavelength vs decay time. **a)** Shows the spectra for TiO_2 sample and TiO_2/BN with visible variation in the <550 regimes. The dashed black line shows the profiling region (600 nm) taken for the kinetics plot. **b)** Kinetics at 600 nm, pump 310 nm, 0.5 mJ/cm^2, red lines show the best fit with mixed first and second-order function with k_1=64 ± 12 ns^{-1} and k_1=3.4 ± 1.2 ns^{-1} for the samples without BN and with BN, respectively (see **Table SI** for the details). The dashed region marks the visible variation in decaying times for samples with BN. **c)** and **d)** show similar studies as presented in a) and b), but extracted for TiO_2/ZnO and TiO_2/ZnO/BN samples, respectively.

Although there is a general change in the overall response of the sample with BN, the most important information for the TiO_2/ZnO/BN and TiO_2/ZnO samples, comes from the longer decay components, shown in **Figure 3b and 3d** for the exemplary kinetics at 600 nm measured at pump energy density 0.5 mJ/cm^2. In the UV-VIS range, the decay of transient absorption signal, associated with the holes population, is similar for all samples at high excitation densities (4 mJ/cm^2, **Figure S7**), but at lower excitation density, the decay becomes significantly longer for the samples with BN (**Figure 3b and 3d**). In NIR range (**Figure S6)** the decay of the signal <1 ps is due to the electrons

in the conduction band and their fast trapping by the shallow traps. The later dynamics in NIR range (due to the recombination of the trapped electrons) is similar for all samples and it remains unchanged for higher and lower energy densities, as shown by the comparative plot of decaying times in **Figure S8**. It suggests that the decay of holes in BN samples is dominated by the second-order radiative recombination **(Table S3)**, while the decay of the electrons in all samples (revealed in NIR range) and the holes in the samples without BN is dominated by the fast first-order trap assisted decay, known as Shockley–Read–Hall recombination[78]. Therefore, it is clear that the introduction of BN and BN bridges, increases the lifetime of holes in the material, due to the decrease of first-order recombination rate via trap states. Furthermore, the obtained average first-order rate of the holes recombination (trap assisted) is 64 ± 12 ns^{-1} for the samples without BN, and more than one order of magnitude lower for the samples with BN, 3.4 ± 1.2 ns^{-1} (**Figure 3, Table S3**). The first-order decay can be associated with the average transit time (τ) for electrons and holes from the interior to the surface. The value of τ can be calculated by [79]: $\tau = d\text{^}2/(\pi\text{^}2\ D)$, were, d – the geometrical parameter (in this case the thickness of the layer) and D – the diffusion coefficient. The estimated ratio of the diffusion coefficient of holes for the samples with (D_1) and without (D_2) BN is $D_1/D_2 \approx 21$. Thus, BN, as an interfacial hole extractor, promotes the more efficient transfer of photogenerated holes towards the surface.

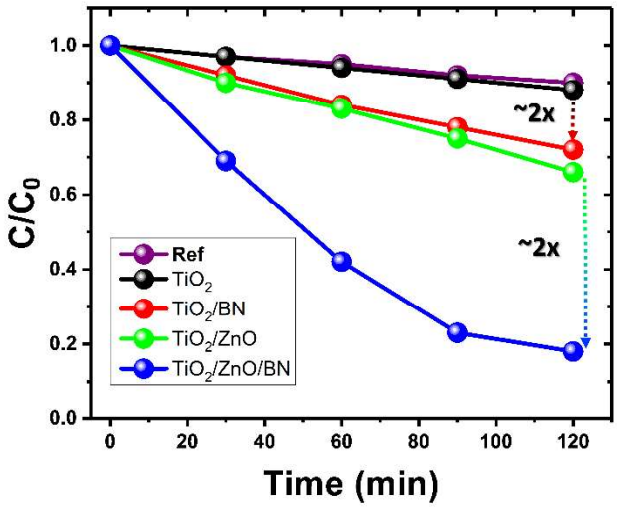

Figure 4: Normalized recorded Photodegradation experiments performed on the whole set of samples. Dashed lines show the increment between similar samples after the inclusion of BN. The ~2X represents the more than 2 fold increment between samples.

3.4 Effect of BN layers on Photodegradation

Degradation efficiency studies were performed on all the samples using Rhodamine 6G. The results of the experiments are shown in **Figure 4**. As expected, the inclusion of BN, increased the

efficiency of all the samples, as shown by the total observed degradation and the estimated photodegradation rate. The photodegradation rate was calculated according to the equation $\ln(C/C_0) = -kt$, where C/C_0 is the normalized degradation recorded, k is the degradation constant, and t the time in minutes. In the case of TiO_2, the total degradation reaches 12% (k=1.01*10^{-3} min^{-1}), which then is doubled by the addition of B-N in the TiO_2/BN sample, with degradation of 28% (k=2.42*10^{-3} min^{-1}). This increment is also observed for TiO_2/ZnO, with a total degradation of 34% (k=2.84*10^{-3} min^{-1}) which is more than doubled by the B-N, as a result, the TiO_2/ZnO/BN sample shows a photodegradation of 82% (k=7.84*10^{-3} min^{-1})

Table 1: BN based composited of TiO_2 - ZnO

	Material (pore size and area)	**Synthesis**	**Bandgap(eV)**	**Current Density**	**Enhancement**	Ref
BN–TiO_2	Porous Composite (43.88 Å and 103.66 m^2g^{-1})	Autoclave/Ice bath method	2.91 (↓)	-	Metyl Blue degradation (73%) vs. (33%) of TiO_2	[80]
BN/TiO_2	Composite nanofibers	electrospinning	3.62 (↑)	-	Methyl Orange degradation (5x than TiO_2)	[51]
F-BN/TiO_2	Porous Composite (43.80 Å and 103m^2g^{-1})	Mechanochemical/Sol-gel	2.66 (↓)	3.0 × 10^{-6} Acm^{-2} (↑) (?V)	Degradation of RhB (92%), MB (90.5) and phenol dyes (78%)	[81]
BN/TiO_2	Porous Hybrid Nanosheets (263 m^2 g^{-1})	Dynamic templating	2.95(↓)	~2.5 × 10^{-6} Acm^{-2} (↑) (0V)	Rhodamine B (99%)	[50]
BN/TiO_2	Nanoparticles (7.0m^2 g^{-1})	Ball milling	3.0 (-)	~45× 10^{-6} Acm^{-2} (↓)	Rhodamine B (~85%)	[82]
BN/TiO_2	Hetero Structure (170 $m^2g^{-1}$and 0.457 cm^3g^{-1})	Solvothermal process	2.88(↓)	~0.14× 10^{-6}A (↑) (0V)	Rhodamine B (~87%)	[53]
BN/TiO_2	Composite nanofibers	electrospinning	2.75(↓)	~0.6× 10^{-6} Acm^{-2} (↓) (0 V)	Ibuprofen (99%)	[83]
BN/ZnO	Polycrystalline Polymorphic nano-microparticles.	Ball milling	(-)	-	Degradation of RhB (82%)and MB (60%)	[84]
BN/ZnO/TiO_2	Flat Heterostructures (30 nm thick)	ALD	3.0(↓)	5.0 × 10^{-6} Acm^{-2} (↑) (0.5 V)	Rhodamine 6G (82%) vs (34%) of TiO_2/ZnO and (12%) of TiO_2	This Study

The arrows, (↑) and (↓) denote increment or diminution with respect to the as-prepared materials. (-) denotes no change.

Finally, it is important to remark that in the literature several architectures have been proposed, many of which profit from the TiO_2 and ZnO composite junction with BN (see **Table 1**). Although most of these studies have shown enhancement of bandgap and current density, the true origin of the enhancement and magnitude remained generally open for debate. Despite it, the consensus pointed to the enhanced carrier separation of the Van der Waals junction, while the B-N

bridges were associated with the bandgap discussion. Here, we have achieved a rather competitive current density, bandgap reduction, and degradation rate, in what is more important, an optically transparent ultra-thin active area (<40 nm). Furthermore, we show conclusive evidence of the dynamics involved in the B-N/ZnO and B-N/TiO_2 systems, although we suspect that it might be similar in other direct bandgap metal oxides. Further studies are needed to determine the level of hybridization and B-N brides vs bandgap reduction on the composites, plus its influence on the carrier lifetime and recombination rate.

Conclusion

In summary, we have not only investigated the general dynamics of B-N composites but also provide a novel photocatalysts material based on TiO_2/BN and TiO_2/ZnO/BN for enhanced photoelectrochemical water oxidation and photodegradation of contaminants. The composite was developed by the ALD technique, providing easy coverage of exposed areas and rather straightforward integration in other architectures. We examined the influence of the BN layer and B-N bridges on the overall photo/electrochemical performance of produced composites. As expected, the introduction of the ALD BN layer can greatly improve the photocatalytic performance of the metal oxide composites. It is apparent that Zn-O-B-N and Ti-O-B-N bridges at the interface of TiO_2/BN and ZnO/BN heterojunctions improve the visible light absorption. This effect is due to the formation of additional energy levels in the forbidden band of metal oxides that was proved by the narrowing of the energy gap from 3.2 to 3 eV. At the same time, the combination of an efficient electron transfer interface (TiO_2/ZnO) and a hole-collector (BN) improves the separation of photogenerated electron and hole pairs in TiO_2 and/or ZnO. As a result, the BN layer can quickly transfer the separated holes to the interface of electrode/electrolyte, and as a consequence, enhancing the PEC efficiency. Furthermore, the TiO_2/ZnO/BN composite shows a high photodegradation rate with 82% (k=7.84*10^{-3} min^{-1}) towards the reduction of contaminants.

The synergistic effect of both mechanisms, such as of B-N bridges and hole extraction, and the large scalability of the here presented method, make the BN produced by ALD a promising candidate for the new class of photoactive materials. Additionally, we conclusively show the role of B-N on the general efficiency of its heterojunctions with a first-order rate of the holes recombination of 64 ± 12 ns^{-1} for the samples without BN, and, 3.4 ± 1.2 ns^{-1} for samples with BN. This work provides a new strategy to develop advanced photocatalytic materials and nanocomposites, and a quantitive mechanism for understanding the enhancement of B-N junctions.

Acknowledgments

E.C: Acknowledges the partial financial support from the National Science Centre (NCN) of Poland by the OPUS grant 2019/35/B/ST5/00248**. E.C, M.B and I.I:** Acknowledge the partial financial support of RISE- H2020-EU.1.3.3. Grant (ID:778157) CanBioSe. **I.I:** Acknowledges the partial financial support from the National Science Centre (NCN) of Poland by the OPUS grant 2020/37/B/ST5/00576. **K.S**: Acknowledges the partial financial support from the National Science Centre (NCN) of Poland by Sonata-BIS no 2017/26/E/ST5/00416. **I.G-K and M.Z**: Acknowledge the partial financial support from the National Science Centre (NCN) of Poland by the Sonata-BIS no 2015/18/E/ST4/00196.

Author Contributions:

All authors have approved the final version of the manuscript.

References

[1] C. Lai, N. An, B. Li, M. Zhang, H. Yi, S. Liu, L. Qin, X. Liu, L. Li, Y. Fu, F. Xu, Z. Wang, X. Shi, Z. An, X. Zhou, Future roadmap on nonmetal-based 2D ultrathin nanomaterials for photocatalysis, Chem. Eng. J. 406 (2021) 126780. https://doi.org/10.1016/j.cej.2020.126780.

[2] Z. Wang, Z. Qi, X. Fan, D.Y.C. Leung, J. Long, Z. Zhang, T. Miao, S. Meng, S. Chen, X. Fu, Intimately Contacted Ni2P on CdS Nanorods for Highly Efficient Photocatalytic H2 Evolution: New Phosphidation Route and the Interfacial Separation Mechanism of Charge Carriers, Appl. Catal. B Environ. 281 (2021) 119443. https://doi.org/10.1016/j.apcatb.2020.119443.

[3] Y. Kim, E. Coy, H. Kim, R. Mrówczyński, P. Torruella, D.-W. Jeong, K.S. Choi, J.H. Jang, M.Y. Song, D.-J. Jang, F. Peiro, S. Jurga, H.J. Kim, Efficient photocatalytic production of hydrogen by exploiting the polydopamine-semiconductor interface, Appl. Catal. B Environ. 280 (2021) 119423. https://doi.org/10.1016/j.apcatb.2020.119423.

[4] S. Chen, G. Ma, Q. Wang, S. Sun, T. Hisatomi, T. Higashi, Z. Wang, M. Nakabayashi, N. Shibata, Z. Pan, T. Hayashi, T. Minegishi, T. Takata, K. Domen, Metal selenide photocatalysts for visible-light-driven Z -scheme pure water splitting, J. Mater. Chem. A. 7 (2019) 7415–7422. https://doi.org/10.1039/C9TA00768G.

[5] Y. Wu, H. Wang, W. Tu, S. Wu, J.W. Chew, Effects of composition faults in ternary metal chalcogenides (Zn In2S3+, x = 1–5) layered crystals for visible-light-driven catalytic hydrogen generation and carbon dioxide reduction, Appl. Catal. B Environ. 256 (2019) 117810. https://doi.org/10.1016/j.apcatb.2019.117810.

[6] A. Rawat, R. Ahammed, Dimple, N. Jena, M.K. Mohanta, A. De Sarkar, Solar Energy Harvesting in Type II van der Waals Heterostructures of Semiconducting Group III